Vol. 9, No. 5, October 2025, pp. 459-467

Current Optics and Photonics

Regular Paper

Diurnal Atmospheric Turbulence Effects on 1.57 μm Ground-to-air Illumination Laser System Performance

Sung Hun Choi[1], Ji Yong Joo[1], Jun Ho Lee[1,2]*, Byung Wan Kim[3], Jun Ho Jung[3], Yung Joong Kim[3], Eun Sook Yoon[4], and Jang Pyo Kim[4]

[1]*Department of Optical Engineering, Kongju National University, Cheonan 31080, Korea*
[2]*Institute of Application and Fusion for Light, Kongju National University, Cheonan 31080, Korea*
[3]*Electro-Optical Team, Hanwha Systems Co., Seongnam 13524, Korea*
[4]*Agency for Defense Development, Daejeon 34186, Korea*

(Received August 6, 2025 : accepted September 3, 2025)

This study investigated the performance degradation of a 1.57 μm ground-to-air illumination laser system under varying atmospheric turbulence conditions. A time- and altitude-resolved simulation framework based on the Hufnagel–Valley model was developed using site-specific measurements of the refractive index structure parameter (C_n^2) collected over one week in March 2025, along with wind speed data from the regional meteorological agency. Received energy was estimated over a full diurnal cycle using a four-step propagation model comprising forward transmission, target interaction, back-scattering, and receiver filtering. Simulation results showed substantial temporal variation in system performance, driven by turbulence fluctuations. The highest return energy occurred at 21:00 (4.38 mW), while the lowest was at 12:00 (1.01 mW), corresponding to a 77% decrease in signal strength and a 129% increase in fluctuation. Although the timing may vary, the results consistently showed maximum returns 2–3 hours after sunset, when turbulence is weakest, and minimum returns around midday, when turbulence peaks. These findings underscore the significant impact of diurnal turbulence on the stability and efficiency of laser-based systems and support the importance of optimized operational scheduling. Future work will focus on experimental validation under comparable atmospheric conditions.

Keywords : Diurnal atmospheric turbulence, Ground-to-air laser system, Laser beam propagation, Refractive index structure function (C_n^2), Turbulence-induced performance degradation
OCIS codes : (010.1080) Adaptive optics; (010.1330) Atmospheric turbulence; (010.3310) Laser beam transmission; (140.0140) Lasers and laser optics

I. INTRODUCTION

Laser beam propagation plays a critical role in various applications, including satellite laser ranging (SLR) [1, 2], optical wireless communication [3, 4], LIDAR [5, 6], and laser power transmission [7]. In these systems, the beam must traverse the atmosphere, where refractive index fluctuations, turbulence, and meteorological variables such as wind and temperature contribute to signal degradation [8, 9]. These effects can induce beam spreading, scintillation, and beam wander, as illustrated in Fig. 1, leading to temporal fluctuations in beam intensity, particularly under strong atmospheric turbulence [10]. Since turbulence intensity varies with both altitude and time, accurate modeling of its impact is essential, especially for systems that require stable and continuous operation.

Several studies in South Korea have investigated the influence of atmospheric conditions on beam propagation, particularly in ground-to-space or near-vertical configurations. As summarized in Figs. 2(a)–2(d), recent efforts

*Corresponding author: jhlsat@kongju.ac.kr, ORCID 0000-0002-4075-3504

Color versions of one or more of the figures in this paper are available online.

pISSN: 2508-7266 / eISSN: 2508-7274 https://doi.org/10.3807/COPP.2025.9.5.459

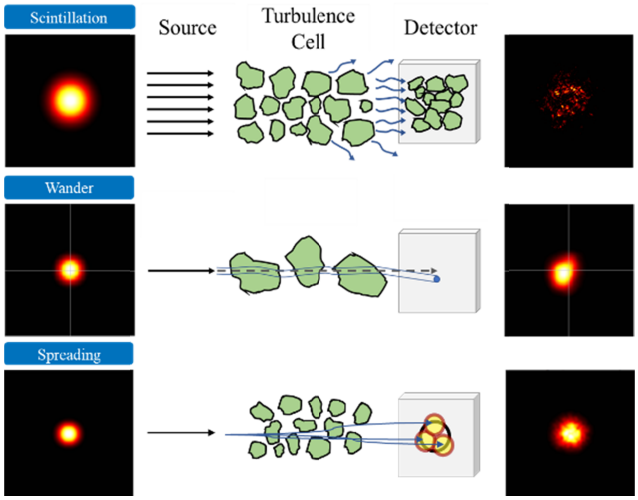

FIG. 1. Atmospheric turbulence effects on laser beams: (top) scintillation causing intensity fluctuations, (mid) beam wander causing centroid displacement, (bottom) beam spreading enlarges the beam due to phase distortions in air.

range from observational to computational and experimental approaches. One example is the development of a SLODAR system at the Geochang SLR Observatory [Fig. 2(a)], which enables multilayer reconstruction of the refractive index structure parameter (C_n^2) up to altitudes of 7.8 km and supports adaptive optics research under Korean environmental conditions [11]. On the computational side, numerical models based on the frozen flow hypothesis have been used to generate time-evolving phase screens by translating turbulence maps according to wind speed profiles for realistic temporal simulations [Fig. 2(b)] [12]. In addition, sensitivity analyses incorporating measured turbulence profiles have quantified the influence of key beam parameters such as wavelength, beam radius, jitter, and beam quality (M^2) on long-distance propagation, and jitter was identified as the dominant factor [Fig. 2(c)] [13]. To complement these efforts, experimental testbeds using rotating phase plates have been developed to emulate Kolmogorov-type turbulence under controlled laboratory conditions for repeatable

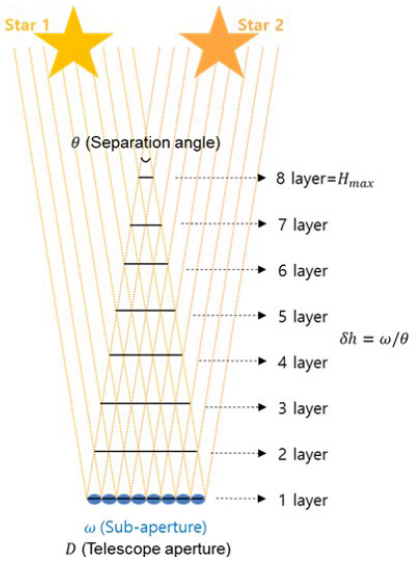

(a)

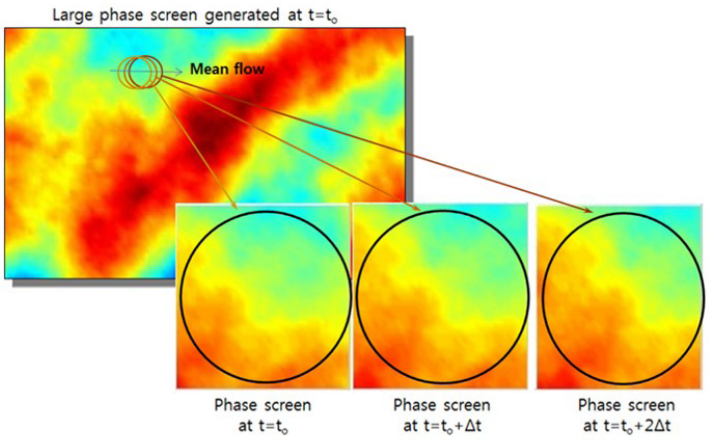

(b)

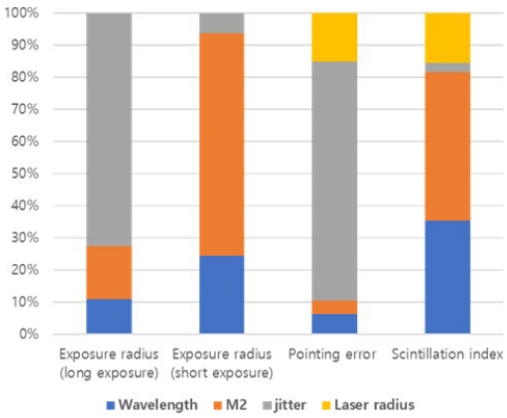

(c)

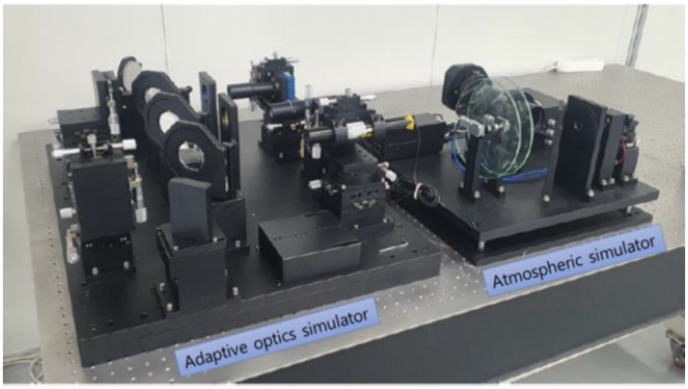

(d)

FIG. 2. Representative approaches to turbulence modeling and compensation: (a) SLODAR-based profiling, (b) frozen-flow simulation, (c) parameter sensitivity analysis, (d) laboratory turbulence emulator.

system-level validation [Fig. 2(d)] [14]. These studies collectively offer complementary tools for characterizing, simulating, and experimentally replicating turbulence-induced beam distortion and form a practical basis for investigating beam propagation under realistic atmospheric conditions.

Despite these advancements, most existing studies rely on static or idealized turbulence assumptions and do not explicitly account for how beam propagation characteristics evolve under real atmospheric conditions throughout the day. Only a few studies have considered beam propagation under time-varying turbulence. This temporal variability is especially important for high-altitude illumination systems operating over extended periods of time, where turbulence dynamics can significantly affect performance stability.

The present study addressed this gap by quantitatively evaluating temporal fluctuations in the energy returned from a high-altitude illuminated target during laser beam propagation [10, 15]. A time–altitude-resolved turbulence model was built using diurnal time-series measurements of C_n^2 acquired by a scintillometer combined with altitude-dependent wind speed profiles derived from rawinsonde data. This model was then integrated into a time-resolved beam propagation simulation to examine how atmospheric variations over a diurnal cycle influenced energy stability. The amplitude and temporal characteristics of these fluctuations were analyzed at selected time intervals to identify dominant trends associated with evolving atmospheric conditions.

This paper is organized as follows: Section 2 describes the experimental setup and turbulence model formulation. Section 3 details the simulation and signal analysis methodology. Section 4 presents and discusses the results, focusing on the dominant environmental factors that influence beam propagation characteristics under time-varying atmospheric conditions.

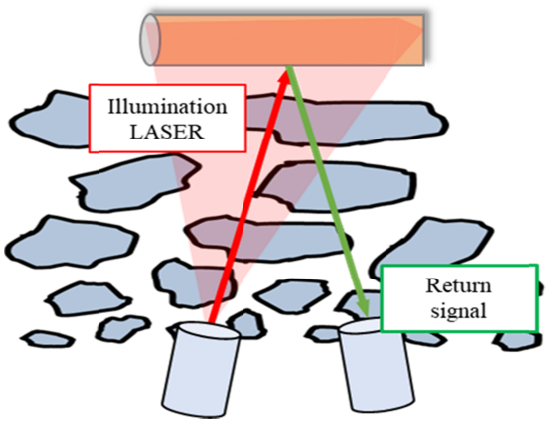

FIG. 3. Conceptual diagram of the laser illumination system. A vertically directed beam propagates from a ground-based transmitter through a turbulent atmosphere, reflects off a high-altitude scattering region, and returns to the optical receiver.

II. TIME-RESOLVED SIMULATION OF LASER PROPAGATION

2.1. Time-resolved Simulation of Return Signal Propagation

This study investigated the temporal behavior of a return signal generated by a vertically projected illumination laser. The term return signal refers to the portion of optical energy that interacts with a high-altitude scattering region after being transmitted upward through the atmosphere and is reflected or scattered back to a ground-based receiver. This two-way propagation is subject to atmospheric turbulence along both the outbound and inbound paths, leading to fluctuations in received energy over time. Figure 3 illustrates the conceptual geometry of the system, in which a laser beam emitted from a ground-based platform propagates upward through turbulent layers, interacts with the target region, and returns along a similarly distorted path to the receiver.

To model this process, a time-resolved beam propagation simulation was developed. The framework consisted of four sequential stages, as shown in Fig. 4. In the first stage, the forward propagation of the laser beam through a vertically stratified turbulent atmosphere was simulated, resulting in a distorted intensity distribution at the target plane. Next, a spatial mask was applied to account for the physical characteristics of the target, such as its shape, reflectivity, and angular spread, thereby determining the subset of the beam that contributes to the return path. The third stage modeled backward propagation using a Lambertian scattering approximation, which assumed isotropic re-radiation from the illuminated region back through the same atmospheric layers. Finally, the returning beam was passed through the receiver aperture, and the total return energy was calculated by integrating the intensity over the receiving area.

Throughout this simulation, the atmospheric conditions were represented using a time-altitude-resolved turbulence model, built from measured values of C_n^2 and wind speed profiles. A laser wavelength of 1.57 μm was used, and the

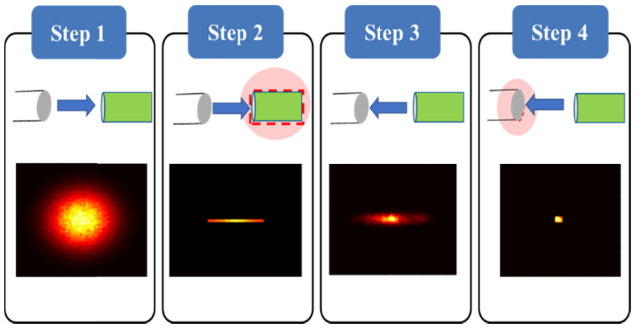

FIG. 4. Stepwise configuration of the vertical laser propagation simulation. The panels illustrate the four simulation stages: (1) Forward beam transmission, (2) target interaction, (3) backward beam transmission, and (4) receiver aperture filtering, along with the corresponding energy distributions at each step.

output power was 4 W, which was not large enough to produce significant thermal blooming effects. The overall simulation approach was adapted from vertical phase screen propagation models originally proposed by Andrews *et al*. [12] and later refined by Lee *et al*. [16], allowing turbulence-induced distortions to be accounted for in both forward and backward directions.

2.2. Atmospheric Turbulence Modeling Based on the Hufnagel–Valley Model

To reflect the altitude-dependent characteristics of atmospheric turbulence, this study adopted the empirical Hufnagel–Valley (HV) model, which estimates C_n^2 as a function of altitude h. The model is given by [12]:

$$C_n^2(h) = A \cdot \exp\left(-\frac{h}{100}\right) + 2.7 \times 10^{-16} \exp\left(-\frac{h}{1500}\right) + 0.00594 \left(\frac{\omega}{27}\right)^2 (10^{-5}h)^{10} \exp\left(-\frac{h}{1000}\right), \quad (1)$$

where h is the altitude (m), ω is the root-mean-squared (RMS) wind speed (m/s), and A is the ground-level value of C_n^2. Using time-series measurements of ground-level C_n^2 and estimated RMS wind speeds, a time- and altitude-dependent turbulence model $C_n^2(h, t)$ was built. The HV model was applied independently at each time step to generate vertical turbulence profiles, which were subsequently used in the simulation to analyze time-varying return energy.

Figure 5 illustrates the sensitivity of the turbulence profile according to key parameters. Figure 5(a) shows the effect of varying RMS wind speed, and Fig. 5(b) shows the impact of different ground-level C_n^2 values A. While the ground-level C_n^2 primarily influences near-surface turbulence, the RMS wind speed has a more pronounced effect in the upper atmosphere.

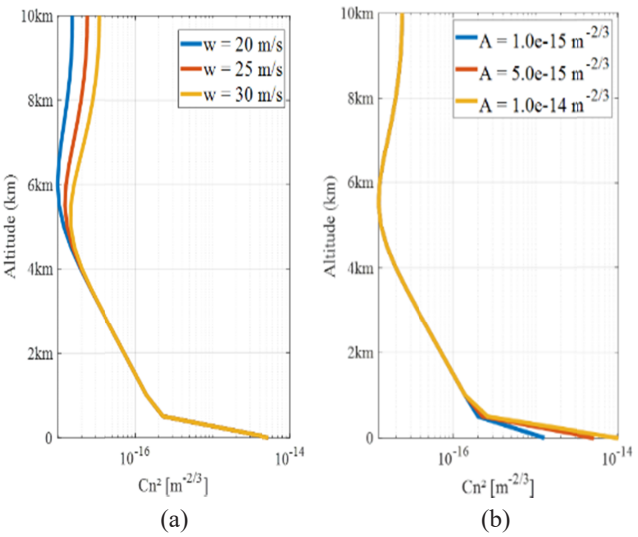

FIG. 5. Vertical profiles of the C_n^2 based on the HV model. (a) Effect of RMS wind speed ω on turbulence strength at $A = 5 \times 10^{-15}$ m$^{-2/3}$. (b) Effect of ground-level C_n^2 value A on turbulence profiles at $\omega = 25$ m/s.

III. DATA-DRIVEN ATMOSPHERIC TURBULENCE MODEL CONSTRUCTION

3.1. Measurement Site and Environmental Conditions

To quantitatively evaluate the temporal variation of received laser energy under realistic atmospheric turbulence, we measured time-varying turbulence strength on the ground over a 1.4 km path with a scintillometer. The measurements were performed in an open-field site in Cheoin-gu, Yongin-si, Gyeonggi-do, South Korea (latitude 37.1341°, longitude 127.1687°). The site was characterized by flat terrain with minimal artificial structures, which provided favorable conditions for natural atmospheric flow and turbulence development. Figure 6 shows the location of the measurement site and a picture of the scintillometer setup at the site. Table 1 summarizes the specifications of the applied scintillometer (Kipp & Zonen B.V., Delft, Netherlands) [17].

A transmitter–receiver pair was deployed along the east–west direction with a separation of approximately 1.4 km, which was selected as the optimal path length for scintillometer-based measurement of the C_n^2. The optical axis of the system was aligned parallel to the ground surface, and both transmitter and receiver were fixed at positions that minimized the influence of heat sources and reflective surfaces.

Measurements were conducted along the fixed 1.4 km

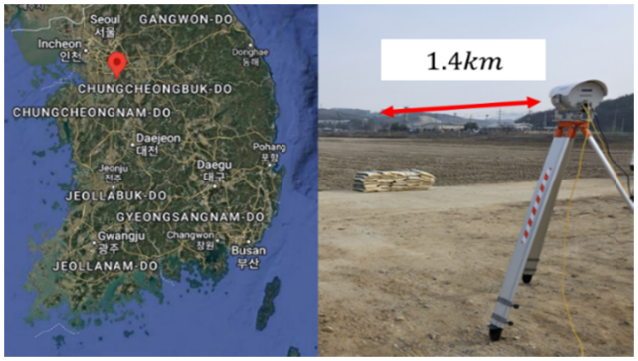

FIG. 6. Location of the measurement site and scintillometer setup over a 1.4 km path.

TABLE 1. Scintillometer specifications [17]

Parameter	Value
Model	LAS MkII
Wavelength (nm)	850
Measurement Range	$10^{-17} - 10^{-13}$ m$^{-2/3}$
Sampling Rate (Hz)	1
Path Length (km)	0.25–4.5 (Optimal: −1–2)

path throughout the full daytime period, from sunrise to sunset. This configuration was designed to simulate the vertical propagation conditions of high-altitude laser operation (10 km) and provide essential input for evaluating turbulence-induced effects on laser beam propagation. Details of the measurement schedule and parameters are presented in the following subsection.

3.2. Measured Parameter: Refractive Index Structure Parameter (C_n^2)

Measurements were conducted continuously over a nine-day period from March 20 to 28, 2025, with daily schedules from before sunrise until after sunset to capture the full diurnal cycle of atmospheric turbulence. A scintillometer was deployed along a 1.4 km horizontal path to measure the refractive index structure parameter C_n^2. The data were recorded at 1-minute intervals and subsequently averaged over one-hour windows to generate a time-series representation of turbulence variation. These hourly averaged values were used as input parameters for the HV model. The resulting diurnal trend of C_n^2 is presented in Fig. 7.

As shown in the figure, C_n^2 remained relatively low and stable at approximately 10^{-15} $m^{-2/3}$ before sunrise. However, beginning around 08:00, turbulence strength increased sharply, reaching values exceeding 10^{-14} $m^{-2/3}$ between 12:00 and 14:00 due to solar-induced surface heating. Following this peak, C_n^2 declined in the late afternoon and returned to lower, more stable levels after sunset.

This diurnal pattern reflects the influence of solar radiation–induced surface heating on the generation of atmospheric turbulence. The ability to quantitatively capture this temporal evolution of turbulence strength is necessary for building time-resolved atmospheric models. In particular, the high-turbulence time window corresponds closely to the period when received energy tends to decrease and fluctuate more significantly. Therefore, accurate modeling of turbulence characteristics during these hours plays a critical role in the time-dependent implementation of the HV model.

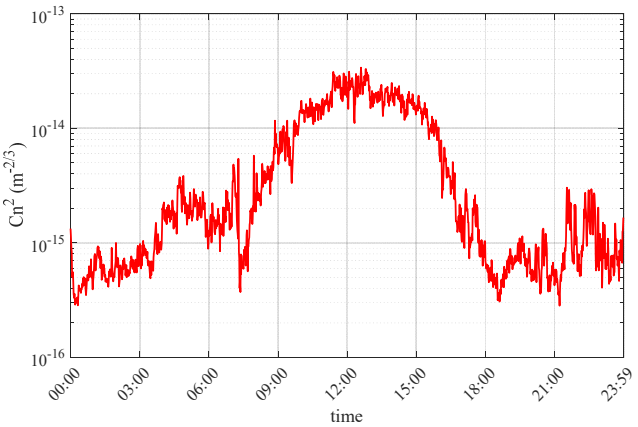

FIG. 7. Time-series C_n^2 measured over 24 hours (23 Mar, 2025).

3.3. Predictive Parameter: Altitude-dependent Wind Speed Modeling

RMS wind speed is defined as [12]:

$$\omega = \left[\frac{1}{h_2 - h_1}\int_{h_1}^{h_2} v(h)^2\, dh\right]^{1/2}, \tag{2}$$

where $v(h)$ is the wind speed at altitude h, and the integration bounds are defined as $h_1 = 5$ km and $h_2 = 20$ km.

Since direct measurements at the site in this range were impractical, we used radiosonde data provided by the Korea Meteorological Administration (KMA) [18]. The KMA measures wind profiles four times a day (0:00, 06:00, 12:00, and 18:00 local time) at 10 sites including the nearest one located 13 km from our measurement site. Since the wind profiles are strongly dependent on the season, we sampled the radiosonde wind speeds of the nearest site in the same season (March to May) over the recent 5 years (2019–2024). Figure 8 plots the wind speeds over altitude at 12:00 local time with a mean profile. Figure 9 plots the calculated RMS wind speeds at the four local times (0:00, 06:00, 12:00, and 18:00) with a fitted line.

3.4. Construction of a Time-resolved HV Model

We applied the time-resolved C_n^2 and RMS wind speeds to the HV model [Eq. (1)]. This enabled the calculation of altitude-dependent C_n^2 profiles and produced a turbulence model that captures daily atmospheric variation. Figure 10 plots the HV model outputs at 0:00, 06:00, 12:00, and 18:00 UTC. While profiles above 5 km remained similar across time, near-ground turbulence increased significantly around 12:00 UTC due to solar surface heating. From the C_n^2 profiles, we calculated the diurnal atmospheric, seeing variations in terms of Fried parameter (r_0) and isoplanatic angle (θ_0), as plotted in Fig. 11.

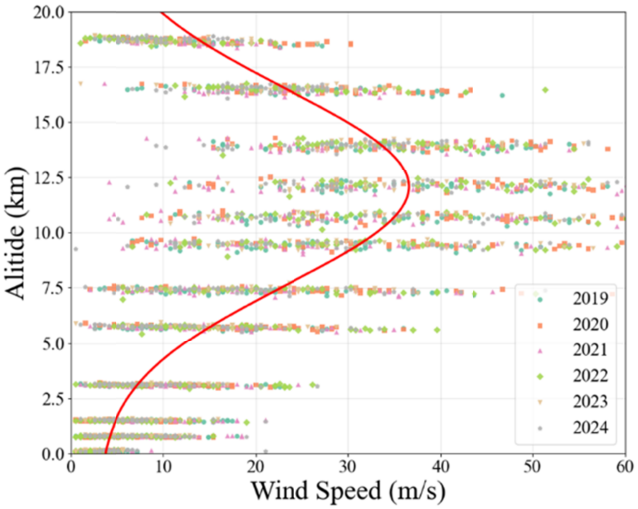

FIG. 8. Wind speed over the altitude at 12:00 local time in spring (March to May) for the recent 5 years (2019–2024), provided by the Korea Meteorological Administration (KMA).

IV. RESULTS AND ANALYSIS

4.1. Overall Simulation Conditions

The beam propagation process was modeled as a four-stage sequence involving: (1) Forward laser transmission through a vertically stratified atmosphere, (2) interaction with a high-altitude target, (3) backscattered beam propagation, and (4) optical filtering at the receiver. This sequence is illustrated in Fig. 4, which visualizes both the physical configuration and the resulting energy distributions at each step.

Atmospheric turbulence effects were incorporated using altitude- and time-resolved phase screens generated from Hufnagel–Valley (HV) profiles. These profiles were updated at three-hour intervals, yielding eight distinct turbulence conditions during a 24-hour cycle. The simulation considered a 10 km vertical propagation path in both directions, with turbulence applied separately to the outbound and inbound paths.

The high-altitude target was modeled as a Lambertian scattering surface with an effective area of 0.45 m^2, centered along the optical axis. The masking process was applied to the beam intensity at the target plane, such that only the optical energy falling within this region was allowed to contribute to the return path. This selective filtering is visualized in Fig. 12(a), which highlights the overlap between the forward-propagated beam and the target surface.

Figure 12(b) shows the received intensity distribution after backscattering and turbulent return propagation. The circular region with a 0.3 m diameter corresponds to the receiver aperture, over which the total energy was spatially integrated to obtain the return signal. This double-stage spatial filtering at both target and receiver levels plays a critical role in determining system performance under time-varying turbulence conditions.

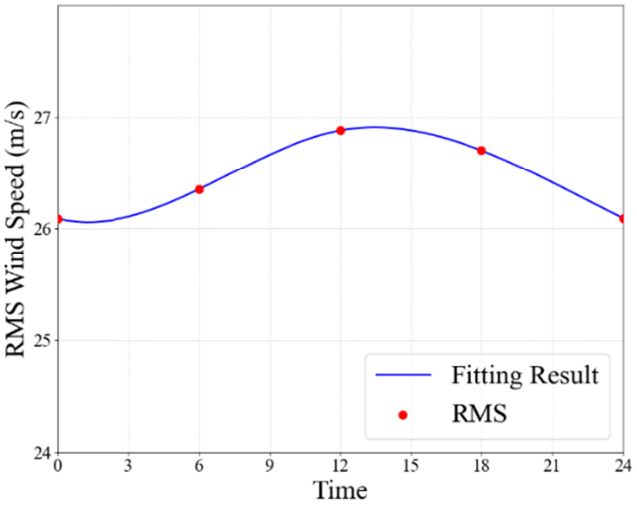

FIG. 9. Calculated RMS wind speeds at four local times (0:00, 06:00, 12:00, 18:00) and its best fit curve.

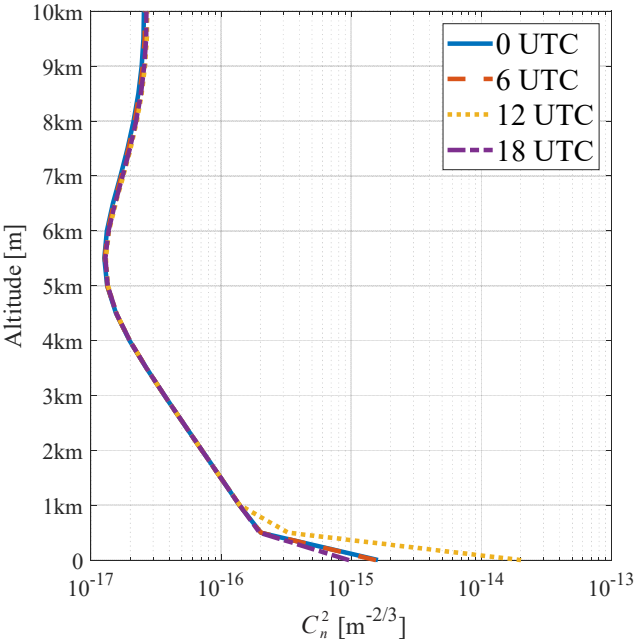

FIG. 10. Time-dependent C_n^2 profiles at 0:00, 6:00, 12:00, and 18:00 UTC. Near-surface turbulence increases around 12:00 UTC.

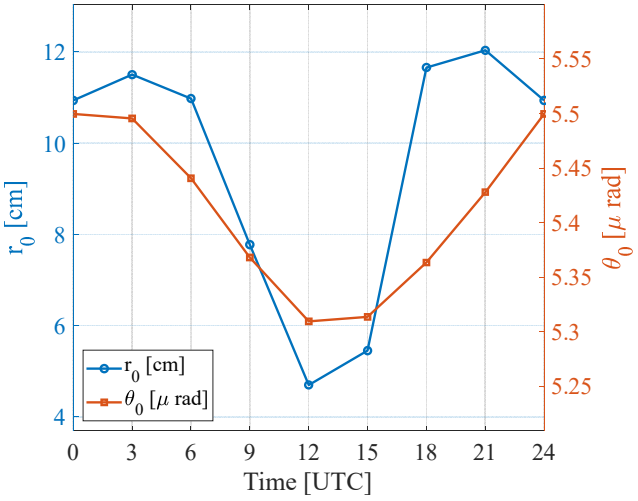

FIG. 11. Diurnal atmospheric seeing variation in terms of Fried parameter (r_0) and isoplanatic angle (θ_0).

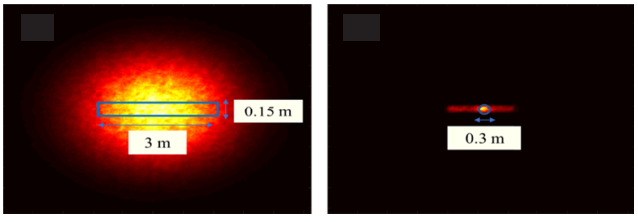

FIG. 12. Beam intensity and backscattered response for a scattering target. (a) Beam intensity at the target plane with a 0.45 m^2 effective scattering area. (b) Received intensity after backscattering, integrated over a 0.3 m aperture.

The key simulation parameters are summarized in Table 2.

4.2. Temporal Variation in Received Energy

Figure 13 shows the hourly variation of the mean received energy over a 24-hour period under varying atmospheric turbulence conditions. The overall trend reflected an inverse relationship between received energy and turbulence strength.

The highest received energy was recorded under the weakest turbulence condition at 21:00 UTC, while the lowest energy occurred under the strongest turbulence at 12:00 UTC. These two cases were designated as the best-case and worst-case conditions, respectively. In the best case, observed at 21:00 UTC, the received energy reached 4.38 mW from an initial transmitted power of 4 W. In contrast, under the worst turbulence condition at 12:00 UTC, the received energy dropped to 1.01 mW. This represents a 77% reduction in collected energy compared to the best case, highlighting the strong dependence of system performance on atmospheric turbulence intensity. This degradation corresponded to the midday intensification of turbulence, driven by solar surface heating, which elevates C_n^2 and causes stronger beam scattering and distortion.

These results demonstrated that atmospheric turbulence significantly degraded laser energy delivery and underscored the importance of incorporating realistic, time-varying turbulence models in performance prediction.

This diurnal pattern, characterized by a sharp degradation in performance during midday and recovery during nighttime, suggested that the most favorable operational window may occur within 2–3 hours after sunset. This temporal alignment coincides with periods of atmospheric stabilization driven by the cessation of solar surface heating. While this trend was observed under the modeled conditions, additional data would be required to determine its general applicability in varying locations or seasons.

TABLE 2. Simulation parameters

Category	Parameter	Value
Laser	Power (W)	4
	Wavelength (μm)	1.57
	Beam Size (cm)	7.5
	M^2	25
	Jitter (RMS) (μrad)	10
Atmosphere	Model	Hufnagel–Valley
	No. of Phase Screens	5 with Equally Spaced
Propagation	Propagation Distance (km)	10
	Propagation Angle (deg)	0 (vertical)
Target	Area (m^2)	0.45
	Surface Model	Lambertian
	Reflectivity (%)	35
Receiver	Aperture Diameter (cm)	30

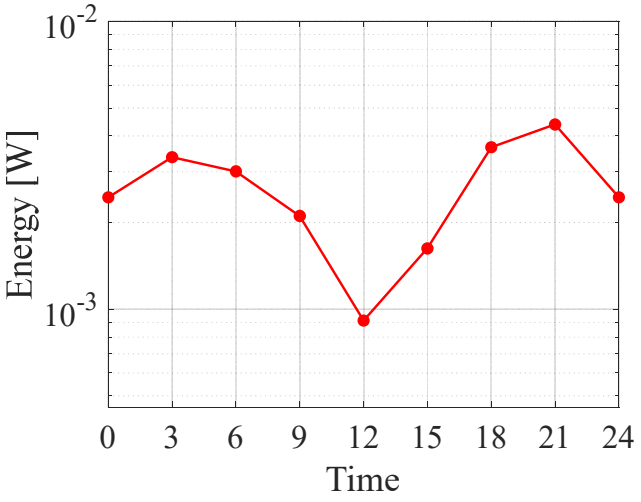

FIG. 13. Hourly variation of mean received energy, showing a 79% drop from 21:00 UTC to 12:00 UTC due to turbulence.

4.3. Distribution Characteristics and Fluctuation of Received Energy

Figure 14 shows the distribution of received energy under best-case (21:00 UTC) and worst-case (12:00 UTC) turbulence conditions. In the best case, the energy was densely concentrated around the mean of 4.38 mW, with a standard deviation of 0.16 mW. This narrow distribution indicated that the received energy remained temporally stable when

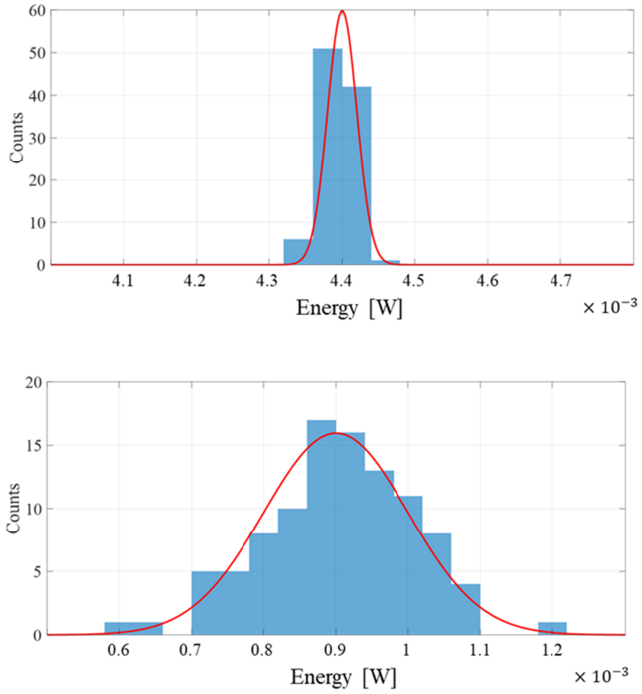

FIG. 14. Received energy histograms at 21:00 UTC (top) and 12:00 UTC (bottom), showing reduced stability and lower mean under strong turbulence.

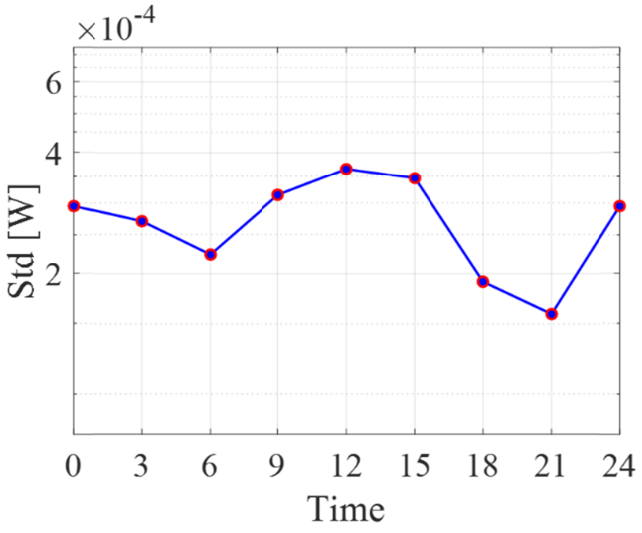

FIG. 15. Hourly variation of standard deviation in received energy. Fluctuation peaks near midday (12:00 UTC) and reaches a minimum around 21:00 UTC, indicating an inverse relationship with turbulence strength.

atmospheric turbulence was weak.

In contrast, the distribution became noticeably broader under worst-case conditions. The standard deviation increased to 0.37 mW while the mean dropped to 1.01 mW, indicating greater variability in received energy due to stronger turbulence. This corresponds to a 129% increase in temporal fluctuation compared to the best case.

These results demonstrated that turbulence intensity not only reduced the mean received energy but also increased its temporal dispersion. Figure 15, showing the hourly trend of standard deviation, supported this observation. The lowest fluctuation occurred at 21:00 UTC and the highest at 12:00 UTC, matching the distribution behavior seen in Fig. 14. This inverse relationship between mean energy and fluctuation underlined the importance of accounting for temporal variability in the performance analysis of laser systems.

V. CONCLUSION

In this study, we developed a time- and altitude-resolved simulation framework to evaluate the impact of diurnal atmospheric turbulence on the performance of a 1.57 μm ground-to-air illumination laser system. The framework incorporated site-specific measurements of the refractive index structure parameter and altitude-dependent wind speed profiles to turbulence models using the Hufnagel–Valley model. With this model, we simulated the temporal variation in received energy over a full 24-hour cycle.

The results indicated that atmospheric turbulence significantly influences both the magnitude and stability of return signals. Specifically, the lowest energy was recorded around midday, while the highest occurred approximately 2–3 hours after sunset, corresponding to periods of reduced thermal activity and increased atmospheric stability. This contrast represented a 77% decrease in signal strength and a 129% increase in temporal fluctuation between the most and least favorable conditions.

These findings suggested that incorporating time-aware operational planning could substantially improve system performance, particularly for laser systems that require continuous or energy-efficient operation. By identifying favorable atmospheric windows based on diurnal turbulence profiles, system scheduling can be optimized to minimize energy loss and signal instability.

While the present simulation was grounded in a specific diurnal dataset, the resulting trends were consistent with well-understood atmospheric dynamics. To further improve the applicability of the model in broader environmental conditions, future work will extend this approach to multiple sites and seasonal datasets to support greater generalization and deployment flexibility. In addition, field experiments using a 1.57 μm illumination laser and comparable receiver configurations are planned in order to directly compare the measured return energies with the simulation results.

FUNDING

This research was supported by the Agency for Defense Development and funded by the government (Defense Acquisition Program Administration) in 2025 as part of the Defense Research and Development Program (UG233031TD).

DISCLOSURES

The authors declare no conflict of interest.

DATA AVAILABILITY

Data underlying the results presented in this paper are not publicly available at this time, but may be obtained from the authors upon reasonable request.

REFERENCES

1. K. Sośnica, D. Thaller, R. Dach, P. Steigenberger, G. Beutler, D. Arnold, and A. Jäggi, "Satellite laser ranging to GPS and GLONASS," J. Geod. **89**, 725–743 (2015).
2. K. Ahn, S.-H. Lee, I.-K. Park, and H.-S. Yang, "Simulation of a laser tomography adaptive optics with Rayleigh laser guide stars for the satellite imaging system," Curr. Opt. Photon. **5**, 101–113 (2021).
3. T. Koonen, K. Mekonnen, Z. Cao, F. Huijskens, N. Q. Pham, and E. Tangdiongga, "Ultra-high-capacity wireless communication by means of steered narrow optical beams," Phil. Trans. R. Soc. A. **378**, 20190192 (2020).
4. I. Rasheed, G. Sodhi, and R. Malhotra, "Optimizing data transmission: Analyzing FSO based DWDM system in turbu-

lent environments," in *Proc. 11th International Conference on Reliability, Infocom Technologies and Optimization (Trends and Future Directions) (ICRITO)* (Noida, India, Mar. 14–15, 2024).
5. T. Fahey, M. Islam, A. Gardi, and R. Sabatini, "Laser beam atmospheric propagation modelling for aerospace LIDAR applications," Atmosphere **12**, 918 (2021).
6. V. A. Banakh and I. N. Smalikho, "Lidar studies of wind turbulence in the stable atmospheric boundary layer," Remote Sens. **10**, 1219 (2018).
7. B. Acherjee, "Laser transmission welding of polymers – A review on process fundamentals, material attributes, weldability, and welding techniques," J. Manuf. Process. **60**, 227–246 (2020).
8. M. Eshagh, *Satellite Gravimetry and the Solid Earth* (Elsevier, Netherlands, 2021).
9. D. Giggenbach and A. Shrestha, "Atmospheric absorption and scattering impact on optical satellite-ground links," Int. J. Satell. Commun. Netw. **40**, 157–176 (2021).
10. L. C. Andrews and R. L. Phillips, *Laser Beam Propagation through Random Media*, 2nd ed. (SPIE, USA, 2005).
11. J. Y. Joo, H. S. Ha, J. H. Lee, D. H. Jung, Y. S. Kim, and T. Butterley, "SLODAR system development for vertical atmospheric disturbance profiling at Geochang observatory," Curr. Opt. Photon. **8**, 30–37 (2024).
12. L. C. Andrews, R. L. Phillips, and C. Y. Young, *Laser Beam Scintillation with Applications* (SPIE, USA, 2001).
13. J. H. Pak, J. Y. Joo, J. H. Lee, J. I. Kim, S. H. Cho, K. S. Park, and E. S. Son, "Evaluating laser beam parameters for ground-to-space propagation through atmospheric turbulence at the Geochang SLR observatory," Curr. Opt. Photon. **8**, 382–390 (2024).
14. I. Toselli, B. Agrawal, and S. Restaino, "Gaussian beam propagation in maritime atmospheric turbulence: Long term beam spread and beam wander analysis," Proc. SPIE **7814**, 78140R (2010).
15. F. Quatresooz, D. Vanhoenacker-Janvier, and C. Oestges, "Computation of optical refractive index structure parameter from its statistical definition using radiosonde data," Radio Sci. **58**, 1–16 (2023).
16. J. H. Lee, J. H. Pak, J. Y. Joo, S. G. Han, Y. Jung, and Y. Kim, "Atmospheric disturbance simulation in adaptive optics: From theory to practice," Korean J. Opt. Photon. **35**, 199–209 (2023).
17. Kipp & Zonen B.V., "LAS MKII Scintillometer," (Kipp & Zonen B.V.), https://www.kippzonen.com/Product/193/LAS-MkII-Scintillometer (Accessed Date: March. 3, 2025).
18. Korea Meteorological Administration, "Rawinsodne," (KMA Weather Data Service: Open MET data portal), https://data.kma.go.kr/data/hr/selectRdsdRltmList.do?pgmNo=49 (Accessed Date: May. 10, 2025).